

Anti-Durotaxis Droplet Motion onto Gradient Brush-Substrates

Russell Kajouri,[†] Panagiotis E. Theodorakis,^{*,†} Jan Židek,[‡] and Andrey Milchev[¶]

[†]*Institute of Physics, Polish Academy of Sciences, Al. Lotników 32/46, 02-668 Warsaw,
Poland*

[‡]*Central European Institute of Technology, Brno University of Technology, Purkyňova
656/123, 612 00 Brno, Czech Republic*

[¶]*Bulgarian Academy of Sciences, Institute of Physical Chemistry, 1113 Sofia, Bulgaria*

E-mail: panos@ifpan.edu.pl

Abstract

Durotaxis motion is a spectacular phenomenon manifesting itself by the autonomous motion of a nano-object between parts of a substrate with different stiffness. This motion usually takes place along a stiffness gradient, from softer to stiffer parts of the substrate. Here, we propose a new design of a polymer brush substrate that demonstrates anti-durotaxis droplet motion, that is droplet motion from stiffer to softer parts of the substrate. By carrying out extensive molecular dynamics simulation of a coarse-grained model, we find that anti-durotaxis is solely controlled by the gradient in the grafting density of the brush and is favorable for fluids with a strong attraction to the substrate (low surface energy). The driving force of the anti-durotaxial motion is the minimization of the droplet–substrate interfacial energy, which is attributed to the penetration of the droplet into the brush. Thus, we anticipate that the proposed substrate design offers new understanding and possibilities in the area of autonomous motion of droplets for applications in microfluidics, energy conservation, and biology.

INTRODUCTION

The spontaneous motion of nano-objects onto substrates has attracted much interest, due to its potential impact in applications, such as microfluidics, microfabrication, coatings, energy conversion, and biology.¹⁻¹² In this kind of autonomous motion, the direction of motion can also be controlled, steered by gradient changes in a substrate property that can be “sensed” by the nano-object. More specifically, such property can be the stiffness of the substrate, which can enable and sustain the motion of the nano-object in a specific direction. A characteristic example here is the motion of cells on tissues, known as durotaxis.¹¹⁻¹⁵ Apart from biological systems, however, durotaxis has also been realised in the case of a spectrum of different nano-objects (*e.g.* fluids), both in theoretical and simulation models,¹⁶⁻²³ as well as in experiments.²⁴

An important aspect of the durotaxis motion is that the nano-object can sustain the motion without external energy supply. However, apart from stiffness gradients, such motion can also be caused by specific substrate patterns. Characteristic examples here are rugotaxis, where the motion of fluids is provoked by a gradient in the wavelength that characterizes wavy substrates,^{25,26} and curvotaxis driven by curved protein complexes at the cell.²⁷ Other possibilities may include the transport of small condensate droplets on asymmetric pillars,²⁸ three-dimensional capillary ratchets,²⁹ or taking advantage of pinning and depinning effects at the three-phase contact line.³⁰ Moreover, in the case of capillary ratchets, the motion can take place along or against the gradient depending on the surface tension of the fluid.²⁹ Wettability gradients have also been exploited to steer the motion of fluids,³¹⁻³³ while the long-range transport of fluids can be realized by using electrostatic^{34,35} or triboelectric charges.³⁶ In contrast, the use of external fields, such as in the case of electrotaxis,³⁷ requires energy supply by an external source, as, also, in the case of thermotaxis to sustain a temperature gradient.³⁸ Other options requiring external sources may include the use of electrical current,³⁹⁻⁴² charge,⁴³⁻⁴⁵ or even simple stretching,⁴⁶ as well as chemically driven droplets,^{47,48} droplets on vibrated substrates⁴⁹⁻⁵² or wettability ratchets.⁵³⁻⁵⁶

In our previous studies, we have investigated various substrate designs that can cause and sustain the motion of liquid droplets,^{16,23,25} which were mainly motivated by relevant experiments.^{24,26} In particular, in the context of durotaxis droplet motion, a new design based on brush polymer substrates was proposed, where the stiffness gradient was imposed by varying the chain stiffness of the grafted polymers along the gradient for a given grafting density.²³ In this case, it has been found that the grafting density of polymer chains and the droplet adhesion to the brush are the key parameters determining whether the motion will be realised, as well as its efficiency. In particular, it has been found that moderate values of both will promote the droplet motion. Surprisingly, the stiffness gradient itself, albeit necessary for the durotaxis motion, turned out to be irrelevant for determining the efficiency of the motion in terms of the average velocity of the droplet. Importantly, the direction of the droplet motion was in the same direction as the stiffness gradient, *i.e.*, from softer to stiffer parts of the substrate. In effect, this translates into a varying substrate roughness, which drives the droplet motion. In contrast, in a specific experiment,²⁴ the direction of motion of droplets on a soft, silicon-gel substrate has been from the stiffer toward the softer parts of the substrate for μm scale droplets, which is well below the capillary length scale (~ 2.5 mm) in the case of water droplets. Although for this reason gravity seems not to play an important role, durotaxis has been more efficient in the case of larger droplets.²⁴ While biological systems^{11–15} and simulation models^{16,17,20,23} have been thus far only able to demonstrate the droplet motion in the direction of the stiffness gradient, that is from softer to stiffer parts of a substrate, to the best of our knowledge, there is currently no *in silico* substrate design that has demonstrated droplet motion in the opposite direction of the stiffness gradient, namely from the stiffer toward the softer parts of the substrate.

Motivated by relevant experiments²⁴ and previous experience with gradient brush substrates,²³ we consider a polymer brush that can initiate and sustain the droplet motion toward the softer parts of the substrate. Here, we will refer to this kind of motion as “anti-durotaxis” in order to underline the fact that the droplet moves in the opposite direction with

respect to a positive stiffness gradient. In this new design of brush substrate, the stiffness gradient is implemented by the gradual change in the grafting density of fully flexible polymer chains. By using extensive molecular dynamics (MD) simulations of a coarse-grained (CG) model, we explore the key parameters of the system, such as the gradient in the grafting density, the droplet attraction to the substrate, the droplet size, and the viscosity. Our method also provides the molecular-scale resolution required to explore the underlying mechanism of the anti-durotaxis motion. In this way, our study casts further light on the self-sustained motion of droplets onto brush gradient substrates, and, as a result, unravels new possibilities in nanoscale science and technology¹⁹ for various medicine and engineering applications.^{12,57} Moreover, brush substrates share structural characteristics with various biological surfaces that can expel various exogenous substances from their structure,⁵⁸ such as the mucus layer from airway epithelia.⁵⁹ Also, in the context of regenerative medicine,¹² the concept of gradient substrates plays an important role for applications in this area, for example, in drug transport within the body. Hence, we anticipate that our study has a broader impact beyond engineering applications. Moreover, since the design of the brush substrate only depends on the variation (gradient) of the grafting density, as compared to a previous design that the chain stiffness and possibly the chemistry of the chains had to be varied to tune the substrate properties,²³ might suggest that the brush system investigated here might hold greater hope for experiments, thus offering further possibilities for relevant applications. In the following, we provide details of the system, simulation model and methodology. Then, we will present and discuss the obtained results, while we will draw the conclusions resulting from our investigations in the final section.

MATERIALS AND METHODS

The system setup is illustrated in Fig. 1. It consists of a brush substrate and a droplet. The brush has a gradient in the grafting density of the polymer chains that are tethered to

a bottom wall of immobile beads with hexagonal (honeycomb) symmetry. Vertical walls of immobile beads at the two ends of the substrate that are parallel to the $y - z$ plane with height $L_w = 15 \sigma$ (σ is the length unit) are also present to support the structure of the brush in the direction of the gradient, extending thus the total area of undistorted grafting density gradient closer to the brush boundaries in x direction.. The droplet is placed on the side with the highest grafting density at a distance 30σ between the center of mass of the droplet and the side wall, as shown in Fig. 1. After examining a range of different scenarios, we have determined that in the current substrate design the droplet motion will take place from higher grafting density areas, which implies a higher substrate stiffness, toward areas of lower grafting density. In the direction of the stiffness gradient (x direction), the length of the substrate is $L_x = 120 \sigma$, while $L_y = 60 \sigma$ is the substrate length in the y direction, as shown in Fig. 1. Periodic boundary conditions are considered in all Cartesian directions. In particular, in the y direction, the boundaries of the simulation box coincide with those of the substrate, while in the x and z directions the size of the simulation box is large enough to prevent the interaction of beads from opposite boundaries. In view of the sufficiently larger simulation box than the substrate in the direction of the gradient (x direction), the presence of the side walls is required in order to maintain the structure of the brush in this direction.

The standard bead-spring model⁶¹ was employed for the molecular dynamics simulations. According to this model, the interactions between the different components of the system, *i.e.*, the drop (d), the brush (b), and the wall (w) beads, are expressed through the Lennard-Jones (LJ) potential, which reads

$$U_{\text{LJ}}(r) = 4\epsilon_{ij} \left[\left(\frac{\sigma_{ij}}{r} \right)^{12} - \left(\frac{\sigma_{ij}}{r} \right)^6 \right], \quad (1)$$

where r is the distance between any pair of beads in the system. The i and j indices in Eq. 1 correspond to the bead type (d, b, w). The size of all of the beads is set to $\sigma_{ij} = \sigma$. Moreover, the LJ potential is cut and shifted at a specific distance (cutoff), which for the interactions

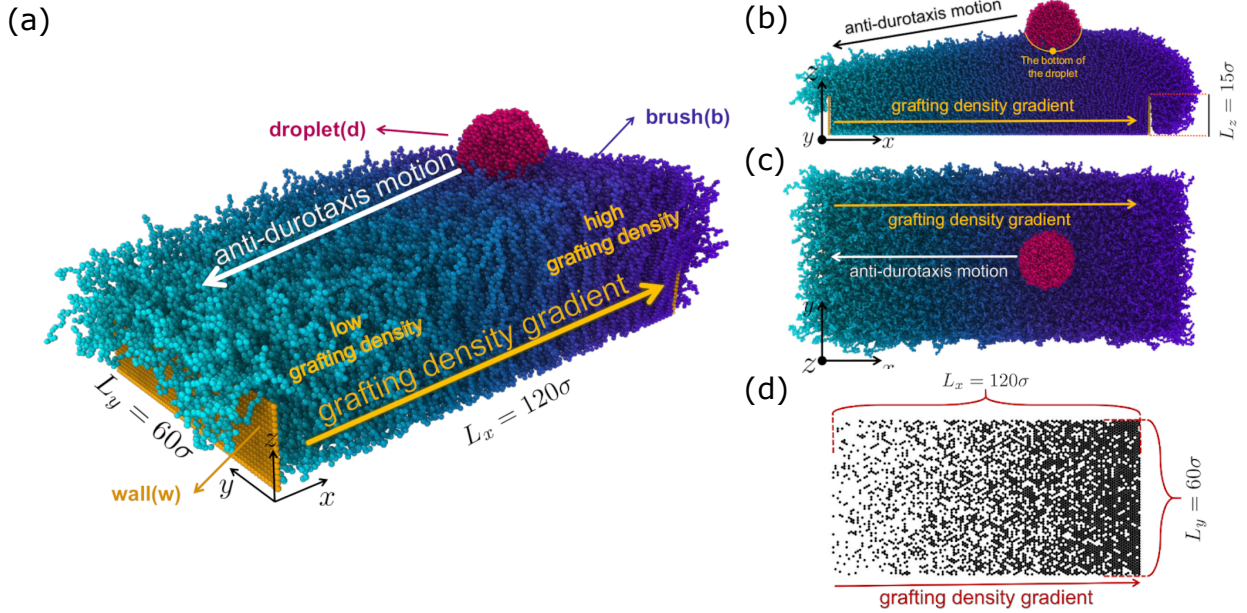


Figure 1: (a) Typical initial configuration of the system. The droplet is placed on the substrate side with the highest grafting density, which is here $\sigma_{g,h} = 0.6 \sigma^{-2}$, while on the other side the lowest grafting density is $\sigma_{g,l} = 0.1 \sigma^{-2}$. The length of the system in the gradient direction, x , is $L_x = 120 \sigma$, with the grafting density gradient defined as $G = (\sigma_{g,h} - \sigma_{g,l})/L_x$. Droplet and substrate polymer-chains consist of fully flexible chains of length $N_d = 10$ and $N_b = 50$ beads, respectively, while the total size of the droplet is $N = 4000$ beads in this case. Also, the strength of the interaction between the droplet and substrate beads is $\varepsilon_{db} = 0.9 \epsilon$. This particular system has shown the most efficient anti-durotaxis motion (in terms of average droplet speed) among all of the cases considered in our study. (b) Side view of the same system after the droplet has moved a certain distance from its starting point. An $x - z$ cross-section passing through the center of mass of the droplet is shown to highlight the penetration of the substrate by the droplet. (c) Top view of the same configuration. (d) The distribution of the grafting sites of the brush polymer chains on the bottom, solid plane of immobile beads with a honeycomb geometry is shown. At the right boundary, chains are randomly grafted in the vertical (y) direction with probability $\sigma_{g,h} = 0.6 \sigma^{-2}$, while $\sigma_{g,l} = 0.1 \sigma^{-2}$ at the left most boundary. The snapshot of the system was obtained using Ovito software.⁶⁰

between the droplet beads or between the droplet and the brush-polymer beads is $r_c = 2.5 \sigma$, while for all other interactions an athermal model is used with the cutoff set to the minimum of the LJ potential, namely $r_c = 2^{1/6} \sigma$. The potential well of the attractive interactions between the droplet beads is $\varepsilon_{dd} = 1.5 \epsilon$, while different choices for ε_{db} are considered for the interaction strength between the droplet and the substrate.⁶² In particular, larger values of ε_{db} would correspond to fluids with smaller surface energy, while smaller values of ε_{db} would

be suitable to model fluids with larger surface energy, *i.e.*, fluids with a lower tendency of wetting a substrate. Here, ϵ is the energy unit and the range $\epsilon_{\text{db}} = 0.1 - 1.2 \epsilon$ is chosen to conduct our investigations, which allows us to capture all possible scenarios for the droplet for the specific substrate design. For all other interactions, such as those between the droplet and the walls or the brush polymers and the walls, the interaction strength is set equal to ϵ , while, as mentioned above, the model is anyway athermal for these repulsive interactions.

The size of the droplet can vary, ranging from 4×10^3 to 16×10^3 beads in our study. These beads are parts of fully flexible, linear polymer chains. While in our investigations the length of the droplet chains is $N_{\text{d}} = 10$ beads throughout the different simulation cases, which ensures that there are no evaporation effects and the vapor pressure is hence sufficiently low,^{23,63} chain lengths of up to 80 beads were also considered for particular cases to explore the effect of viscosity on the anti-durotaxis motion.^{16,23} While the exact value of the viscosity is not of importance here, and while the scaling of the viscosity with the chain length in the model seems not to have been completely settled in the literature, we can however note that the viscosity is expected to grow with the chain length. Moreover, a linear growth with the Kuhn length for Brownian models of melts has been observed on the basis of Rouse dynamics⁶⁴ or a power-law relation $[\eta] = KM^\alpha$ according to Mark–Houwink–Sakurada, with M being the molecular weight of the polymer and K is determined by the intrinsic properties of the used polymer, while $\alpha = 0.8$ for a good-solvent system⁶⁵. Hence, we expect that in melt conditions the viscosity shall grow with a power-law exponent lower than unity for the lengths considered here, while entanglement effects are expected to also play a role for longer polymer chains. Having said that, the viscosity depends on the particular conditions (*e.g.*, solvent conditions) when measured, but it is generally expected to increase with the chain length N_{d} of the chains. The length of the tethered brush polymers, which are of linear molecular architecture, is N_{b} , and remains the same in all of our *in silico* experiments. Based on preliminary tests, we found that this choice allows us to remove any significant dependence of the results on the choice of the brush length, N_{b} , which is also in line with

our previous experience with brush substrates.²³

To tether the beads together in each polymer chain of the droplet or the brush, the finitely extensible nonlinear elastic (FENE) bond potential was applied for consecutive pairs of beads in each chain, which mathematically is expressed as follows:

$$U_{\text{FENE}}(r) = -0.5K_{\text{FENE}}R_0^2 \ln \left[1 - \left(\frac{r}{R_0} \right)^2 \right]. \quad (2)$$

In the above relation, r is the distance between the beads pair and $R_0 = 1.5 \sigma$, which determines the highest possible extension of the bond. $K_{\text{FENE}} = 30 \epsilon/\sigma^2$ is an elastic constant.

The stiffness gradient is realized by varying the grafting density of the polymer chains in the x direction. By considering a hexagonal symmetry of the possible grafting sites on the bottom substrate of immobile beads, chains are randomly grafted to satisfy the required grafting density in the x direction (Fig. 1d). In particular, the substrate is divided into bins with length 3σ along the x direction. At the one end of the substrate we impose the highest grafting density $\sigma_{\text{g,h}}$ in units of σ^{-2} , while at the other end the lowest grafting density is denoted as $\sigma_{\text{g,l}}$. A linear gradient in the grafting density between the two opposite ends is considered, namely $G = (\sigma_{\text{g,h}} - \sigma_{\text{g,l}})/L_x$. After conducting extensive preliminary investigations with different choices for $\sigma_{\text{g,h}}$ and $\sigma_{\text{g,l}}$, we have concluded that setting $\sigma_{\text{g,l}} = 0.1 \sigma^{-2}$ gives us the highest number of successful anti-durotaxis cases, that is, cases that the droplet is able to cross against the gradient the whole distance from the one end of the substrate to the other. This comes as an advantage when investigating the influence of various parameters, such as the droplet size, viscosity or adhesion strength, since more data of successful anti-durotaxis cases can be acquired for the analysis. Finally, the range $\sigma_{\text{g,h}} = 0.4 - 0.9 \sigma^{-2}$ was considered for the highest grafting density of the systems. Lower values of $\sigma_{\text{g,h}}$ would result in small gradients, which would prevent the anti-durotaxis motion. The choice $\sigma_{\text{g,h}} \geq 1.0 \sigma^{-2}$ already imposes large steric effects between the polymer chains and

their close-packing, which would also practically imply small stiffness gradients experienced by the droplet. We have also examined systems with stiff polymer chains for the brush and concluded that anti-durotaxis motion was more efficient in the case of fully flexible brush chains (no angle potential along each brush chain). This is mainly due to a smaller range of possibilities for the stiffness gradient of the substrate when individual polymer chains are stiffer. In addition, stiff chains prevent the penetration of the substrate by the droplet, which, as will become apparent later, hinders the anti-durotaxis motion. Hence, all of the results presented in this study will refer to brush substrates with fully flexible polymer chains.

To control the temperature of the system, $T = \epsilon/k_B$ (k_B is Boltzmann's constant), the Langevin thermostat was used.⁶² Moreover, the coordinates of each bead $\{\mathbf{r}_i(t)\}$ evolve in time by integrating the Langevin equation by means of the HOOMD-Blue package,⁶⁶ which mathematically reads:

$$m \frac{d^2 \mathbf{r}_i}{dt^2} = -\nabla U_i - \gamma \frac{d\mathbf{r}_i}{dt} + \Gamma_i(t). \quad (3)$$

Here, m is the mass of the beads, which is equal to m , with m being the mass unit. t denotes the time, U_i is the total potential acting on the i -th bead, γ is the friction coefficient, and $\Gamma_i(t)$ is the random force. As is well-known, γ and Γ are related by the usual fluctuation–dissipation relation

$$\langle \Gamma_i(t) \cdot \Gamma_j(t') \rangle = 6k_B T \gamma \delta_{ij} \delta(t - t'). \quad (4)$$

Following previous work,^{62,67,68} the friction coefficient was chosen as $\gamma = 0.1 \tau^{-1}$. Equation 3 was integrated using an integration time step of $\Delta t = 0.005 \tau$, where the time unit is $\tau = (m\sigma^2/\epsilon)^{1/2}$. Given the choice of the Langevin thermostat, the simulations are in practice carried out in the canonical statistical ensemble. For each set of parameters, we obtained an ensemble of thirteen statistically independent trajectories by changing the initial velocities assigned to each particle in order to acquire reliable statistics for the analysis of the results. The length of each trajectory was 10^8 MD integration-steps, unless the droplet managed to reach the side of the substrate with the lowest grafting density before the set maximum sim-

ulation time. In this case, the simulation is terminated and the particular case is considered as a successful anti-durotaxis case.

RESULTS AND DISCUSSION

In the case of the durotaxis motion onto a brush, we have determined that the key parameters of the substrate design for a droplet of a given size are the strength of droplet attraction to the substrate and the grafting density.²³ Surprisingly, we have also found that the stiffness gradient, albeit necessary to cause the durotaxis motion of the droplet, was not *per se* key for determining the efficiency of the motion in terms of the time the droplet had required to transverse the full length of the substrate in the simulation. Following a similar protocol in the case of the anti-durotaxis phenomenon, which includes an extensive exploration of the parameter space relevant for the new brush design, we find that the grafting density at the soft end of the substrate should be small, namely $\sigma_{g,l} = 0.1 \sigma^{-2}$. In addition, by investigating a relevant range of systems with different chain stiffness, we have determined that the most efficient anti-durotaxis motion occurs when the brush chains are fully flexible. Henceforth, all of the presented results will therefore consider $\sigma_{g,l} = 0.1 \sigma^{-2}$ and fully flexible polymer chains. By taking this into account, the key parameters determining the efficiency of the anti-durotaxis motion are the stiffness gradient, which is defined by the value of the grafting density at the stiffest (highest grafting density) end of the substrate with grafting density, $\sigma_{g,h}$, and the droplet-brush attraction strength, which is controlled by the LJ parameter ε_{db} .

Figure 2 summarizes the results of the simulations in the form of regime maps with $\sigma_{g,h}$ and ε_{db} as parameters. Different scenarios for the behavior of the droplet are possible during the simulations, *i.e.*, its detachment from, or its full penetration into the brush, a diffusion- or random-walk-like motion, and, finally, anti-durotaxis motion. In particular, the detachment of the droplet takes place for low attraction strength ε_{db} . Due to the thermal fluctuations the droplet is not able to permanently stick to the substrate, which is more probable to happen

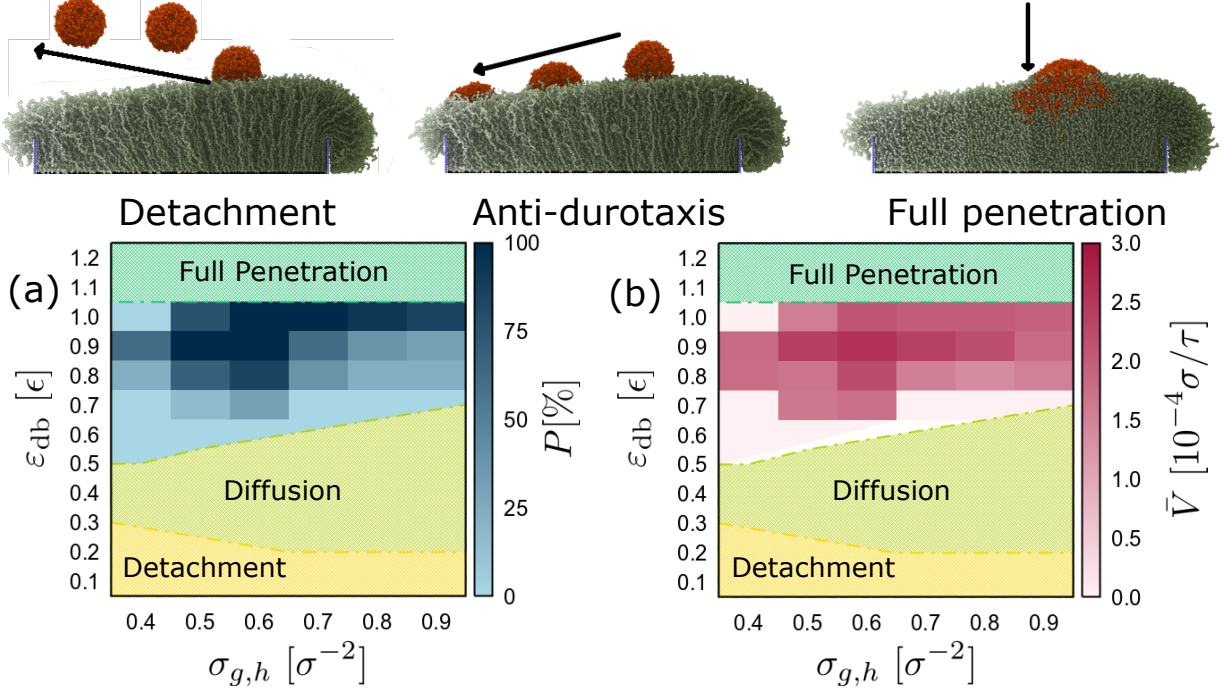


Figure 2: (a) Regime map indicating the probability, P (color scale), that a droplet will cover the full distance over the substrate in the x direction from the stiffest (highest grafting density) to the softest (lowest grafting density) part of the substrate (successful anti-durotaxis case) for different values of the droplet–substrate attraction, ε_{db} , and the highest grafting density, $\sigma_{g,h}$. The lowest grafting density always has the same value, namely $\sigma_{g,l} = 0.1 \sigma^{-2}$. The probability, P , is calculated from an ensemble of thirteen independent simulations for each set of parameters, ε_{db} and $\sigma_{g,h}$. The regimes that the droplet immediately penetrates into the brush and is not able to further move (“Full Penetration”), detaches from the brush due to the weak droplet–brush attraction (“Detachment”), or carries out a random walk onto the substrate (“Diffusion”) are also shown with a different color. (b) The color map indicates the average velocity of the droplet, $\bar{v} = L'_x/t$, for the successful durotaxis cases, where t is the time that the droplet needs to cross the full length of the brush substrate in the x direction, and L'_x is the actual distance covered by the center-of-mass of the droplet for each successful case. $N = 4000$, $N_d = 10$, and $N_b = 50$ beads. Snapshots on top of the plot indicate examples of detachment, anti-durotaxis, and penetration. For the sake of providing a perspective of the various processes, in the former two cases, a time sequence of droplet snapshots at different times are shown (during this time sequence, the configuration of the brush substrate also changes with time, but a single visualization of the brush substrate is shown here only for demonstration), while in the latter case a single snapshot of a cross-section view for the droplet in the brush is illustrated. The snapshot of the system was obtained using Ovito software.⁶⁰

when the grafting density is lower, due to a smaller number of droplet–substrate bead-pair interactions. Moreover, we observe that the dependence on the grafting density disappears

beyond a certain threshold, namely $\sigma_{g,h} \gtrsim 0.6 \sigma^{-2}$, which might imply that the brush density at the interface has reached an adequately high value. In contrast, full penetration takes place when $\varepsilon_{db} \geq \epsilon$, irrespective of the grafting density, which suggests that full penetration be determined by the strong microscopic interactions between the substrate and the droplet beads. In this case, the droplet shape is significantly distorted by the brush chains to the extent that brush chains penetrate through the droplet chains leading to a “non-coherent” droplet (see snapshot of Fig. 2). In the third scenario, the droplet exhibits a diffusion-like (random-like) motion onto the substrate, which takes place for low ε_{db} values. This refers to unsuccessful anti-durotaxis cases that are not able to cross the full length of the substrate in the x direction, that is in this case the driving force of the motion is very weak. Moreover, the range of ε_{db} that such a behavior is observed increases when the grafting density $\sigma_{g,h}$ increases, which already suggests that denser brushes would hinder the possibility of anti-durotaxis motion. In contrast, the decreasing grafting density promotes the motion, and the specific reasons for this will become clearer later, when we will discuss the underlying mechanism of the anti-durotaxis phenomenon.

Anti-durotaxis motion is observed for $\varepsilon_{db} \geq 0.7 \epsilon$, which suggests that a relatively high wettability of the brush by the droplet favor the motion. Moreover, we were able to find anti-durotaxis for the whole range of the grafting density gradients shown in Fig. 2a, but a moderate choice of the highest grafting density, in the range $0.5 \sigma^{-2} \leq \sigma_{g,h} \leq 0.7 \sigma^{-2}$ (the optimum choice of the grafting density on the soft end is $\sigma_{g,l} = 0.1 \sigma^{-2}$), generally presents a high certainty for successful anti-durotaxis motion with high efficiency in terms of the time required to move from the one end to the other end of the substrate. By examining more carefully this time and based on this calculate the average velocity of the droplets during the droplet motion (Fig. 2b), we find that the optimum choice is $\sigma_{g,h} \geq 0.6 \sigma^{-2}$ and $\varepsilon_{db} = 0.9 \epsilon$ when the droplet size is $N = 4000$ beads (Fig. 3).

The results of Fig. 3a indicate that increasing ε_{db} initially renders the droplet motion more efficient in terms of the average droplet velocity, but further increase, namely $\varepsilon_{db} = \epsilon$,

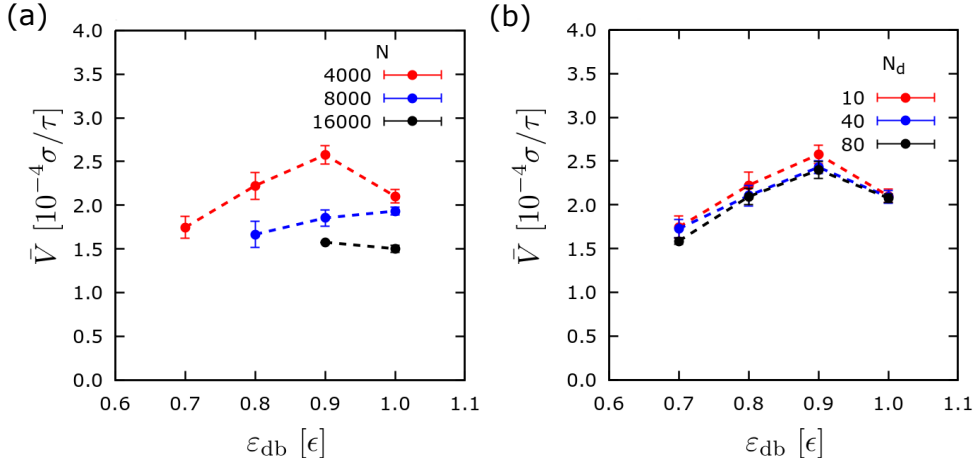


Figure 3: (a) Average velocity of the droplet, \bar{v} , as a function of the attraction strength, ϵ_{db} , for successful anti-durotaxis cases for different droplet size, N , as indicated. The average velocity of the droplet is, $\bar{v} = L'_x/t$, where t is the time that the droplet needs to cross the full length of the brush substrate in the x direction, and L'_x is the actual distance covered by the center-of-mass of the droplet for each successful anti-durotaxis case. $\sigma_{g,h} = 0.6 \sigma^{-2}$, $\sigma_{g,l} = 0.1 \sigma^{-2}$, $N_d = 10$ and $N_b = 50$ beads. (b) The average velocity for different chain lengths N_d of the droplet, as indicated. $\sigma_{g,h} = 0.6 \sigma^{-2}$, $\sigma_{g,l} = 0.1 \sigma^{-2}$, $N_d = 10$, $N_b = 50$, and $N = 4000$ beads.

leads to a smaller velocity. The latter is attributed to the partial penetration of the brush chains into the droplet due to the strong attraction, while for $\epsilon_{db} > \epsilon$ we enter the “full penetration” regime (Fig. 2) and the droplet motion cannot take place. As the droplet size increases, average velocities are evidently lower than those reported in the case of droplet size with $N = 4000$ beads. However, it would be difficult to identify any trends with ϵ_{db} for the larger droplets, since the increase of the droplet size leads to a smaller number of successful anti-durotaxis cases. For example, while the choice $\epsilon_{db} = 0.7 \epsilon$ yields successful anti-durotaxis motion, this choice does not show any success for droplets with size of either $N = 8000$ or $N = 16000$ beads. A final notice concerns the behavior as the droplet viscosity increases (Fig. 3b). Our results indicate that its effect is rather minor, since a similar behavior is observed for the droplets with chains of different N_d for different choices of attraction strength ϵ_{db} . However, less viscous droplets (*e.g.*, $N_d = 10$ beads) appear to slightly favor the anti-durotaxis motion, but differences are rather within a statistical uncertainty. Finally,

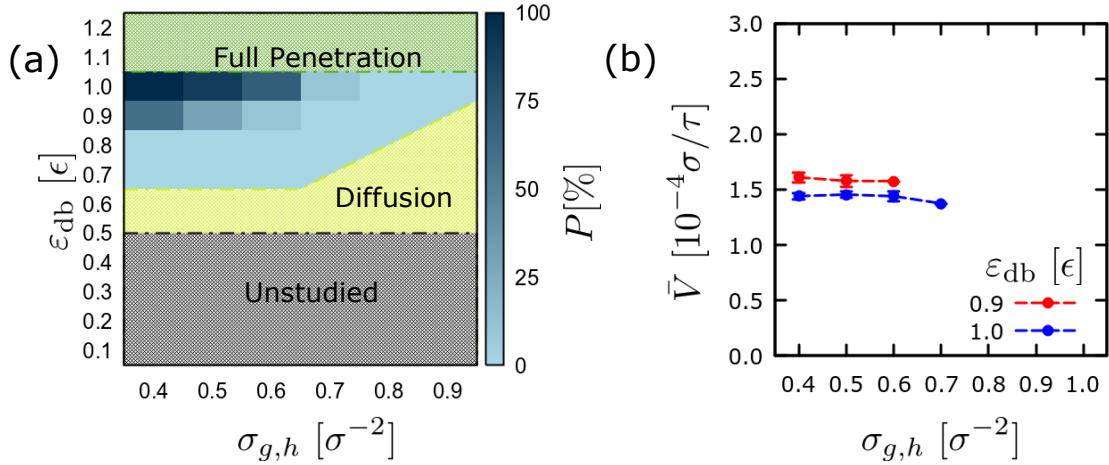


Figure 4: (a) Same as in Fig. 2a, but results are shown for cases that the droplet consists of $N = 16000$ beads in total. (b) Average velocity, \bar{v} , for different gradients as defined through $\sigma_{g,h}$ for two different values of ϵ_{db} for which successful anti-durotaxis motion takes place. $\sigma_{g,l} = 0.1 \sigma^{-2}$, $N_d = 10$ and $N_b = 50$ beads.

a decrease in the velocity for $\epsilon_{db} = \epsilon$ is observed, which is again attributed to the partial penetration of the brush chains into the droplet. Interestingly, this effect appears to be independent of the chain length and fully attributed to the microscopic interactions between the substrate and the droplet beads.

To carefully investigate the effect of the droplet size, we conducted extensive *in silico* experiments with a larger droplet, namely $N = 16000$ beads. Figure 4 presents results for this droplet size, which generally confirm the aforementioned observations. Furthermore, the regime map, which is again based on the parameters ϵ_{db} and $\sigma_{g,h}$, shows that only a few combinations of these parameters were able to lead to successful anti-durotaxis motion, and, moreover, among them, only the set of parameters $\epsilon_{db} = \epsilon$ and $\sigma_{g,h} = 0.4 \sigma^{-2}$ was successful in 100% of our *in silico* experiments. In addition, we observe that smaller values of $\sigma_{g,h}$ favor the anti-durotaxis motion in the case of the droplet with $N = 16000$ beads, in comparison with the case of $N = 4000$ beads (Fig. 2). This suggests that larger droplets require a much softer substrate in order to penetrate into the brush during the anti-durotaxis motion. Also, for both larger and smaller droplets, we observe that anti-durotaxis is favored by larger

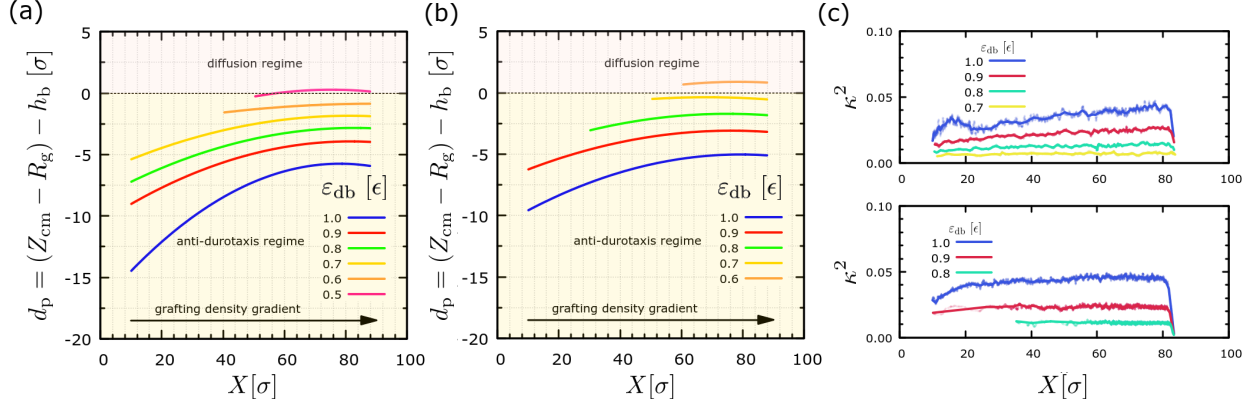


Figure 5: Penetration depth, d_p , of the droplet into the substrate as a function of the X coordinate of the center-of-mass of the droplet along the gradient (the direction of increasing X is toward the regions with higher grafting density, while anti-durotaxis motion is towards smaller X positions of the droplet) for different strength of attraction ϵ_{db} , as indicated. Here, $\sigma_{g,h} = 0.6 \sigma^{-2}$, $\sigma_{g,l} = 0.1 \sigma^{-2}$, $N_d = 10$ and $N_b = 50$ beads. Results for droplet size $N = 4000$ (a) and $N = 16000$ beads (b) are shown. (c) The dependence of the shape anisotropy parameter κ^2 as a function of X for droplets with $N = 4000$ (upper panel) and $N = 16000$ beads (lower panel). See text for details regarding the definitions of d_p and κ^2 .

values of ϵ_{db} . By examining the velocity for the successful cases of $\epsilon_{db} = 0.9 \epsilon$ and $\epsilon_{db} = \epsilon$ (Fig. 4b), we see that the average velocity remains independent of the choice of ϵ_{db} and that the motion is slightly more efficient when $\epsilon_{db} = 0.9 \epsilon$. Hence, only a narrow range of ϵ_{db} values can lead to successful anti-durotaxis motion when the droplet size is $N = 16000$ beads. Also, the range of $\sigma_{g,h}$ for successful motion is more limited in the case of larger droplets. In summary, our data hint that more space is needed within the brush to accommodate the droplet. This will become more apparent during a more detailed discussion of the motion mechanism below.

Visual observations of successful anti-durotaxis cases (for example, see the snapshots in Fig. 2 and movie in the Supporting Information) have led to the suspicion that the droplet gradually immerses into the brush as it moves toward the regions of lower grafting density (softer regions), since the droplet can be accommodated much easier among the brush chains. Hence, a logical next step is to attempt to characterize the degree of penetration of the droplet into the brush during the droplet motion, as part of the anti-durotaxis mechanism. Moreover,

it would be desirable to identify the boundaries between anti-durotaxis motion and other cases, such as diffusive (non-anti-durotaxis or random) droplet motion. The penetration depth serves this purpose here and is defined as $d_p := (Z_{\text{cm}} - R_g) - h_b$, where Z_{cm} is the center-of-mass position of the droplet in the z direction, R_g its radius of gyration, and h_b the height of the brush, which is identified by the inflection point of its density profile $d\rho^2/dz^2 = 0$ within the bin that the X position of the center-of-mass of the droplet belongs. Hence, the penetration depth d_p expresses the degree of the droplet immersion into the brush, since $d_p = -h_b$ when $Z_{\text{cm}} = R_g$, *i.e.*, the bottom of the droplet just touches the top of the brush. In turn, one can rescale the values of d_p according to h_b , and a value of zero would simply reflect the brush surface. Figure 5 presents our results for d_p for different cases, which clearly show that the droplet penetrates deeper into the brush as it moves to areas of lower grafting density (smaller X) during anti-durotaxis. Moreover, the droplet immersion is deeper as ε_{db} increases. This initially correlates with a higher velocity (Fig. 3) of the droplet, but further increase of ε_{db} , namely $\varepsilon_{\text{db}} = \epsilon$, leads to a slower anti-durotaxis motion, despite the difference of the average velocity between $\varepsilon_{\text{db}} = 0.9 \epsilon$ and $\varepsilon_{\text{db}} = \epsilon$ being rather small. When the size of the droplet increases (for example, see Fig. 5b, where plotted data are for droplet with $N = 16000$ beads), the conclusions remain the same, but the drop in the penetration length during anti-durotaxis is much smaller than in the case of droplet with $N = 4000$ beads, which reflects a weaker effect of the gradient and a lower efficiency of motion in the case of larger droplets (for example, see Fig. 3). Overall, the data indicate that successful anti-durotaxis motion is strongly related to the droplet penetration into the brush.

As the droplet penetrates deeper into the brush and moves toward softer areas (smaller grafting density) in successful anti-durotaxis experiments, it is relevant to investigate how the droplet shape changes during the motion. Here, we measured the shape anisotropy, κ^2 , of the droplet as a function of the position X of the droplet center-of-mass. In particular, $\kappa^2 = [b^2 + (3c^2/4)]/R_g^4$ with $R_g = \sqrt{\lambda_x^2 + \lambda_y^2 + \lambda_z^2}$, and $\lambda_x^2, \lambda_y^2, \lambda_z^2$ the eigenvalues of the inertia tensor for the droplet beads. b is the asphericity defined as $\lambda_z^2 - (\lambda_x^2 + \lambda_y^2)/2$ and

c the acylindricity defined as $\lambda_y^2 - \lambda_x^2$. The expectation is that κ^2 obtains values closer to zero for a spherical symmetry and unity in the case of a cylindrical one. The results of Fig. 5c indicate that the droplet initially transforms into a quasi spherical-cap droplet as it is deposited onto the substrate, which manifests itself by the “sharp” increase in κ^2 and generally maintains this symmetry throughout the anti-durotaxis motion with κ^2 however remaining small throughout the motion. Also, the droplets appear to have more spherical shapes for smaller values of ε_{db} . Moreover, as the droplet moves to the regions with lower grafting density, it gradually acquires a slightly more spherical symmetry, due to the softness of the substrate and the more available space in these regions, despite, as we will see later, the higher number of interaction bead-pairs with the surrounding brush polymer chains. Since these interactions are at the substrate–droplet interface (no full penetration as the one defined in Fig. 2), they mainly minimize the energy of the system through the droplet immersion into the brush rather than leading to changes in the elastic energy of the droplet.

In Fig. 6a, we closer examine the brush properties without placing the droplet on the different substrates, thus providing further evidence for our previous arguments. Our results indicate that the height of the brush, h_{b} , decreases toward the regions with lower grafting density (smaller X). This trend does not depend on the particular gradient in the grafting density (different values of $\sigma_{\text{g,h}}$ with $\sigma_{\text{g,l}} = 0.1 \sigma^{-2}$ remaining constant). Hence, the slope of the curves in Fig. 6a is similar. However, larger values of the grafting density directly correlate with a larger height of the brush for a given X position according to the known expression $h_{\text{b}} \sim N_{\text{b}} \sigma_{\text{g}}^{1/3}$.⁶⁹ Examining the density profiles for a particular case with a specific gradient of the grafting density (inset of Fig. 6a), we can also observe how the brush surface transforms from a sharper to a wider interface as we examine density profiles toward regions of lower grafting density. Hence, not only the average height, h_{b} , of the brush changes, but, also, the structure of the interface, which sets favorable conditions for the penetration of the droplet into the substrate. To complete the picture and better understand the above aspects, we have placed a droplet of $N = 4000$ beads onto brush substrates of different

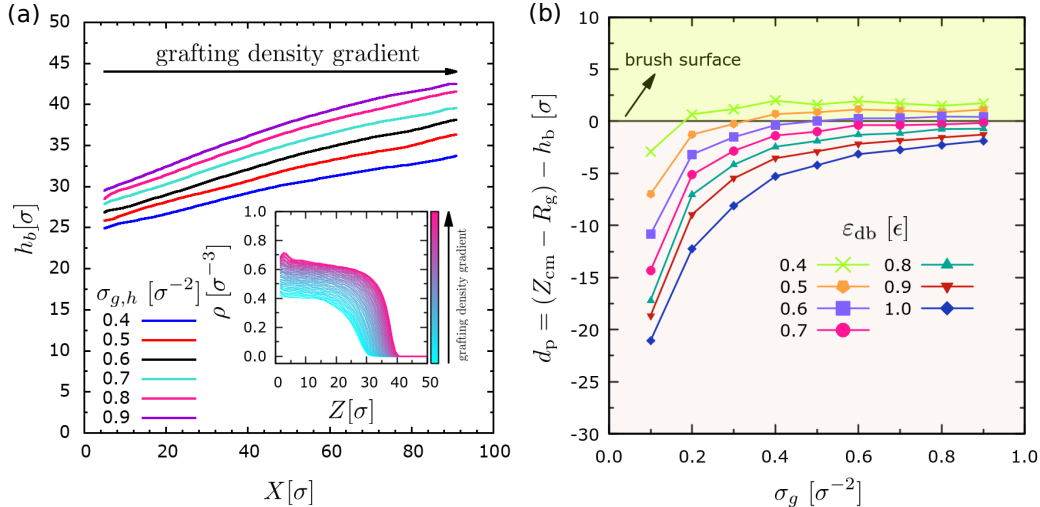


Figure 6: (a) Brush height, h_b , calculated by the inflection point of the number-density profile, $d\rho^2/dz^2 = 0$, along the x direction at each position X for brush substrates with different gradients as defined by the different $\sigma_{g,h}$. In this case, the substrate is simulated without the droplet. Also, increasing X values correspond to areas with larger grafting density. Inset shows the number-density of the beads, ρ , in the direction normal to the brush substrate (z) along the stiffness gradient (different color) for the case $\sigma_{g,h} = 0.6 \sigma^{-2}$. (b) Depth of penetration of the droplet, d_p , into substrates *without* gradient of different grafting density σ_g , as indicated. Data for different droplet–substrate attraction strength ε_{db} are shown. In the case of (a) and (b), data refer to cases with $N_d = 10$, $N = 4000$, and $N_b = 50$ beads.

grafting density, σ_g , and *without* gradient in the grafting density of the chains, and varied the strength of the attraction between the droplet and the brush (Fig. 6b). Then, we measured the penetration depth, d_p . First, we confirm that the droplet will penetrate deeper into the brush when the grafting density becomes smaller. From the point of view of *in silico* nanoindentation experiments, a larger penetration depth reflects a softer substrate.⁷⁰ In the case of substrates with larger grafting density, d_p decreases and rather reaches a plateau when $\sigma_{g,h} > 0.4 \sigma^{-2}$. This suggests that smaller effects be expected in the droplet motion when the gradient becomes larger by setting $\sigma_{g,h}$, and this might explain the lower efficiency of anti-durotaxis motion for larger gradients in the grafting density (Fig. 2). Second, we observe that larger droplet–substrate attraction also leads to a larger penetration depth. This effect seems to be proportional to the attraction strength for a given grafting density. Moreover, small values of ε_{db} and larger grafting density leads to situations where the droplet

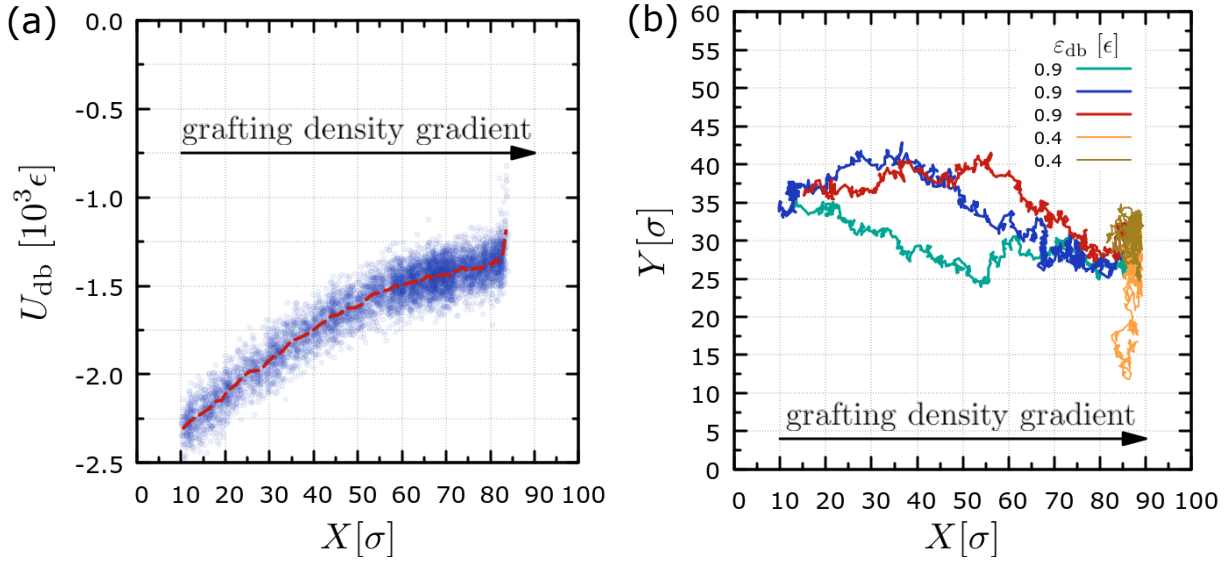


Figure 7: (a) Interfacial energy between the droplet and the substrate, U_{db} , as a function of the position of the center-of-mass of the droplet, X , in the x direction. (b) Typical trajectories of the center-of-mass positions X and Y of the droplet on the $x - y$ plane. Trajectories for $\varepsilon_{db} = 0.9 \epsilon$ refer to successful anti-durotaxis cases with different initial conditions based on a different velocities distribution, while data for $\varepsilon_{db} = 0.4 \epsilon$ correspond to trajectories of diffusive/random droplet motion. The droplet beads in each case have different initial velocities. In both (a) and (b), $N = 4000$, $N_d = 10$, and $N_b = 50$ beads, $\sigma_{g,l} = 0.1 \sigma$, and $\sigma_{g,h} = 0.6 \sigma$. $\varepsilon_{db} = 0.9 \epsilon$ in panel (a).

practically levitates on top of the brush. These cases indicate a weak attraction of the droplet to the substrate. One may assume that these will not cause anti-durotaxis motion, since this kind of motion is strongly driven by the interfacial interactions between the droplet and the substrate, which we will further expand upon below.

In previous studies,^{16,17,23} it has been determined that the minimization of the interfacial energy, U_{db} , is the driving force for durotaxis motion, which is confirmed for different substrate designs.²⁵ Hence, it is also relevant for our study to examine how the droplet–brush interfacial energy varies during the anti-durotaxis motion. Figure 7 presents results of the interfacial energy, U_{db} , as a function of the center-of-mass position of the droplet, X , for a typical anti-durotaxis case. The results confirm that the interfacial energy of the droplet decreases as it moves from the higher grafting density regions to the lower ones. As we have seen already above, this also correlates with a deeper immersion of the droplet into the

brush, which indicates that the penetration of the brush by the droplet sets the conditions for the energy minimization of the system. Furthermore, the energy profile is characterized by an initial smaller slope in the decrease of the energy as a function of the position X of the center-of-mass of the droplet, and then by a larger slope, which correlates well with the results of the penetration depth (Fig. 5), d_p , and indicates that the driving force increases in the softer parts of the brush. In these softer parts, we also observe that the driving force remains constant until the completion of the anti-durotaxis motion, as manifested by the constant gradient, $F_x = \partial U_{db}/\partial x$, which is seen when approximately $X < 60 \sigma$. By monitoring various trajectories of successful anti-durotaxis cases for a particular set of parameters (Fig. 7b), we can clearly see that the motion of the droplet as viewed from the top ($x - y$ plane of the brush) initially appears more diffusive (random) and then much more forward-moving, thus closely reflecting the observations regarding the driving force in Fig. 7a. For the sake of comparison, we also show cases of unsuccessful anti-durotaxis attempts for low ϵ_{db} values, where droplets show a random motion around the very initial position X of the droplet on the substrate. This further indicates that anti-durotaxis motion is not governed by random fluctuations, but it is a result of the particular choice of a set of parameters leading to a driving force, F_x , as in previous *in silico* experiments.²³ In our case, the key set of parameters is specifically the gradient in the grafting density given the choice $\sigma_{g,1} = 0.1 \sigma^{-2}$ and the choice of materials for the brush and the droplet, which will eventually determine the strength of interaction between these two system components.

In the following, we explore the effect of the system temperature on the anti-durotaxis motion. A case of highest motion efficiency is chosen to facilitate the analysis and the temperature of the system is varied. Overall, we find that anti-durotaxis motion will take place for all of the three temperatures studied here (one temperature lower and another greater than ϵ/k_B). Moreover, we monitor the penetration depth and calculate the average velocity of the droplet center-of-mass, with results being presented in Fig. 8. We find that the motion becomes more efficient (on average droplet moves faster) in the case of the lowest

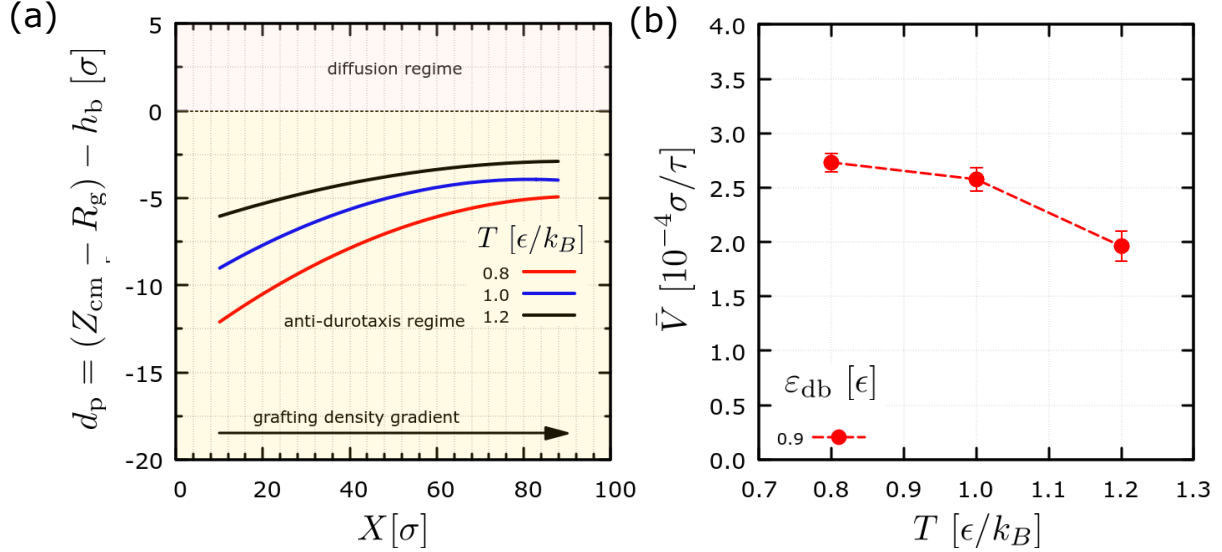


Figure 8: (a) Penetration depth, d_p , as a function of the position, X , of the center-of-mass of the droplet for different system temperature, T , as indicated. (b) Average velocity of the droplet as a function of the temperature. Here, $N = 4000$, $N_d = 10$, and $N_b = 50$ beads. $\epsilon_{\text{db}} = 0.9 \epsilon$ and $\sigma_{\text{g,h}} = 0.6 \sigma^{-2}$. Data are based on an ensemble of 13 independent trajectories for each set of parameters to obtain sufficient statistics.

temperature (Fig. 8b). Moreover, we find that the more efficient motion correlates well with a larger penetration depth of the droplet and a larger slope of the depth as the droplet moves toward the regions with smaller grafting density (Fig. 8a). Hence, we may argue that the anti-durotaxis motion be more efficient at lower temperatures, when thermal fluctuations are less pronounced in the system, and crucially at the droplet–substrate interface, which provides further evidence on the underlying mechanism of the droplet motion, that is the minimization of the droplet–substrate interfacial energy as the droplet is able to establish a larger number of interaction contacts with the brush during anti-durotaxis motion. Note that the brush chains do not penetrate into the droplet chains, and therefore, anti-durotaxis is fully controlled by the interfacial interactions, as in the case of another brush-substrate design.²³ The increase of the temperature generally leads to a decrease in the surface tension of the droplet. However, temperature is also expected to affect the substrate properties. Hence, the synergistic effect of the temperature can only accurately be assessed by simulating

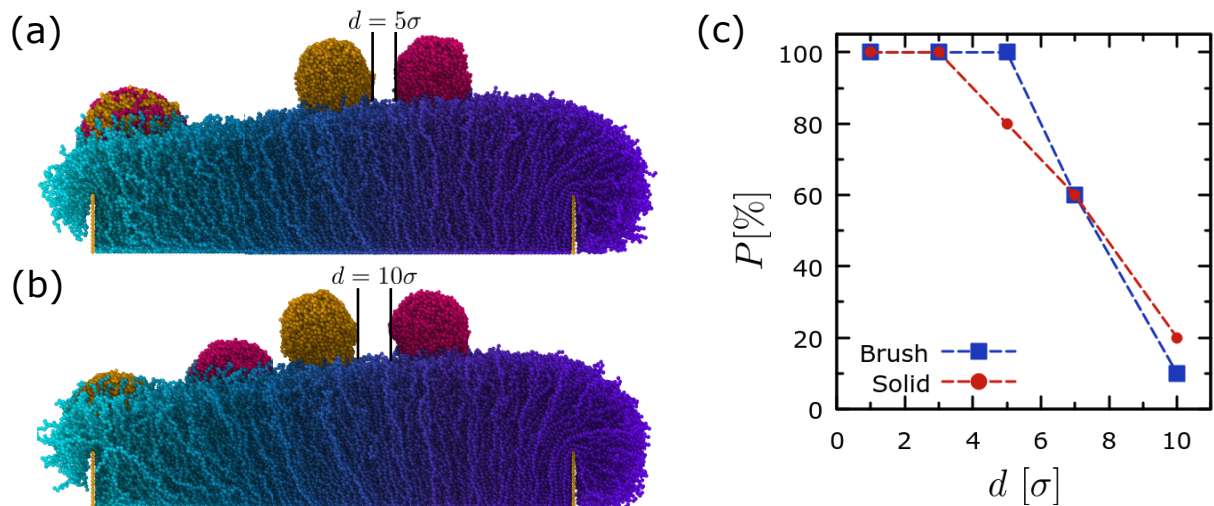


Figure 9: Anti-durotaxis motion of two droplets, which are initially placed at a closer distance (*i.e.*, 5σ) and coalesce (a) and at a larger distance (*i.e.*, 10σ) avoiding coalescence (b). In (a) and (b), the same snapshot has been used in each case, since the substrate is only used for visualization purposes (see videos in Supporting Information for more representative examples.) In both (a) and (b) the snapshots of the droplets are taken at an initial time and at a later time when both (a) or at least one (b) droplet has reached the substrate end with the lowest grafting density. (c) Probability that droplets coalesce as a function of the initial distance between the droplets, d . An ensemble of ten independent trajectories has been considered for the analysis. Here, $N_d = 10$, $N_b = 50$, and $N = 4000$ beads. $\epsilon_{db} = 0.9\epsilon$, $\sigma_{g,h} = 0.6\sigma^{-2}$, and $\sigma_{g,l} = 0.1\sigma^{-2}$. The snapshot of the system was obtained using Ovito software.⁶⁰

systems at different temperature, as is done in our study.

Although the study of a single droplet on gradient substrates offers advantages for *in silico* experiments, for example, isolating the various effects and carefully investigating the droplet–substrate interactions, multiple droplets on the same substrate are often used to carry out the studies in real experiments.²⁴ This might be of benefit, for example, gathering statistics over a larger number of droplets within an individual experiment. While the focus of this study is on the anti-durotaxis motion of a single droplet, we also performed *in silico* experiments with two droplets and carried out an ensemble of ten trajectories for each case to explore the behavior of the system in such a scenario. Again, the most efficient case was chosen for the investigations with results presented in Fig. 9. Here, the main focus

is placed on the role of the substrate in the coalescence of the droplets, in other words to probe whether the brush would favor the droplet coalescence by acting as a “bridge” between the droplets given the softness of the substrate, or the brush chains would rather act as a “barrier” that prevents the coalescence of the droplets. To answer this question, we place two droplets at different distances between each other onto two different substrates, namely the brush substrate with gradient of Fig. 9 and a smooth, unstructured substrate without gradient modeled by a 12–6 LJ potential assuming the same set of interaction parameters. We find that the droplets will first coalesce and then move together as a larger droplet due to anti-durotaxis when the distance is small enough in the case of the brush substrate. Moreover, the probability of coalescence depends on the distance d between the droplets with the brush substrate favoring coalescence over slightly larger distances in comparison with the case where the droplets are placed on the solid substrate. In particular, for $d \leq 3 \sigma$, both substrates will lead to droplet coalescence with 100% probability. The solid substrate then will provide droplet coalescence with a smaller probability and after a distance $d \geq 6 \sigma$ the probability is more or less the same for both substrate types. Since the potential cutoff is 2.5σ , this might suggest that the solid, smooth, unstructured substrate not favor coalescence when the droplets are not able to “feel” each other. In contrast, the brush substrate gives 100% probability of coalescence even when the distance between the droplets is 5σ , which is twice the cutoff distance of the potential. We might argue that the brush chains in this case fill in the space between the droplets and act in favor of coalescence. Further increase of the initial distance between the droplets, d , however, will weaken this effect and the behavior of the droplets in terms of coalescence is the same for both the solid and the brush substrate. Finally, we find that when coalescence between the droplets is avoided, it will not take place later during the anti-durotaxis motion of the droplets (Fig. 9b, see also Supporting Information for the coalescence and noncoalescence cases of Fig. 9). It would be interesting to explore systems with multiple droplets in the future and attempt to further estimate the role of the brush chains as mediators between the droplets or explore synergistic effects that

might be relevant in the anti-durotaxis motion in systems of multiple and diverse droplets, but this clearly goes beyond the scope of the current study.

CONCLUSIONS

In this study, we have proposed and investigated a new design of a brush substrate that is able to lead to the self-sustained motion of droplets without an external energy source. An important difference of this substrate is that the droplet motion takes place in the opposite direction of the stiffness gradient, hence the term anti-durotaxis that is coined in our work. As such, to the best of our knowledge, this is the first time that anti-durotaxis motion has been observed in simulations, since previous cases were mainly concerned with durotaxis motion, that is droplet motion in the direction of the stiffness gradient, from softer to stiffer regions of a substrate.^{16,17,23} Also, durotaxis motion is usually observed in experiments in the lab and biological systems,^{11–15} while anti-durotaxis motion has only been observed for a particular experimental setup.²⁴

As in the case of durotaxis onto brush substrates,²³ our analysis here confirms that the minimization of the interfacial energy constitutes the driving force that underpins the anti-durotaxis phenomenon. However, in the case of anti-durotaxis, this minimization is caused by the gradual penetration of the droplet into the brush as the droplet moves to the softer parts of the substrate with lower grafting density. We have also conducted a parametric study in order to gain further insights into the influence of the various system parameters. We have concluded that soft brushes are in general more suitable for anti-durotaxis, therefore fully flexible polymer chains and the lowest grafting density on the one end of the substrate were always kept $\sigma_{g,1} = 0.1 \sigma^{-2}$. Then, the two key parameters defining the probability of success and the efficiency of the motion in terms of the average droplet velocity are the gradient in the grafting density and the droplet–brush attraction strength. In particular, we find that large values of the droplet–brush interaction strength (low surface

energy) favor the anti-durotaxis motion, when full penetration of the droplet is avoided, namely $\varepsilon_{\text{db}} = 0.9 \varepsilon$ approximately. Then, moderate values of the grafting-density gradient are preferable, in particular $\sigma_{\text{g,h}} = 0.6 \sigma^{-2}$. This is due to the requirement of maintaining the substrate softness that allows its penetration by the droplet while maintaining a highest possible gradient, *i.e.*, a highest possible driving force. As the droplet size increases smaller gradients are performing better, but the anti-durotaxis motion overall is less efficient in the case of larger droplets. The temperature also plays an important role. We find that a lower temperature will favor the anti-durotaxis motion, which provides further evidence supporting the minimization of the droplet–substrate interfacial energy as the driving force of anti-durotaxis. Finally, we find that the viscosity has a minor effect on the anti-durotaxis droplet motion, as it has been also observed in the case of the durotaxis motion for a different brush–substrate design.²³

The key element of the new brush design is the gradient in the grafting density, and therefore it might be more applicable in the case of experiments, since chemically same type of monomers can be used for all chains. Hence, our findings might motivate further experimental research in the area of self-sustained fluid motion onto brush gradient substrates. This might be combined with experiments that include population of droplets, which may provide further understanding of the underlying mechanisms of anti-durotaxis. Here, we have also found that brush substrates favor the coalescence of droplets placed at a close distance in comparison with smooth, unstructured, solid substrates. Another aspect that may require further investigation in the future is to assess possible effects of capillary wave-like fluctuations along the brush surface by simulating much larger systems. We expect that future studies will provide experimental evidence to the plethora of possibilities unfolding regarding anti-durotaxis motion. Also, we anticipate that this study already highlights new possibilities in the design of gradient substrates and, as the first anti-durotaxis *in silico* design, holds important implications for various technological areas, as it aims at forging understanding of the underlying mechanisms that underpin this and similar phenomena.

Acknowledgement

Authors thank Piotr Deuar, Rachid Bennacer, and Sergei Egorov for helpful discussions. This research has been supported by the National Science Centre, Poland, under grant No. 2019/35/B/ST3/03426. A. M. acknowledges support by COST (European Cooperation in Science and Technology [See <http://www.cost.eu> and <https://www.fni.bg>] and its Bulgarian partner FNI/MON under KOST-11). We gratefully acknowledge Polish high-performance computing infrastructure PLGrid (HPC Centers: ACK Cyfronet AGH) for providing computer facilities and support within computational grant no. PLG/2022/015512.

Supporting Information Available

M1*.mp4: Movie illustrates an example of anti-durotaxis motion onto a gradient brush substrate. The parameters for the system are: $N = 4000$, $N_d = 10$, and $N_b = 50$ beads. $\sigma_{g,h} = 0.6 \sigma^{-2}$, $\sigma_{g,l} = 0.1 \sigma^{-2}$, and $\varepsilon_{db} = 0.9 \epsilon$.

M2*.mp4: Movie illustrates a different view of the system in M1*.mp4.

M3*.mp4: Movie illustrates the case of Fig. 9a.

M4*.mp4: Movie illustrates the case of Fig. 9b.

References

- (1) Srinivasarao, M.; Collings, D.; Philips, A.; Patel, S. Three-dimensionally ordered array of air bubbles in a polymer film. Science **2001**, 292, 79–83.
- (2) Chaudhury, M. K.; Whitesides, G. M. How to Make Water Run Uphill. Science **1992**, 256, 1539–1541.
- (3) Wong, T.-S.; Kang, S. H.; Tang, S. K. Y.; Smythe, E. J.; Hatton, B. D.; Grinthal, A.;

- Aizenberg, J. Bioinspired self-repairing slippery surfaces with pressure-stable omniphobicity. Nature **2011**, 477, 443–447.
- (4) Lagubeau, G.; Le Merrer, M.; Clanet, C.; Quéré, D. Leidenfrost on a ratchet. Nat. Phys. **2011**, 7, 395–398.
- (5) Prakash, M.; Quéré, D.; Bush, J. W. Surface tension transport of prey by feeding shorebirds: The capillary ratchet. Science **2008**, 320, 931–934.
- (6) Darhuber, A.; Troian, S. Principles of microfluidic actuation by modulation of surface stresses. Annu. Rev. Fluid Mech. **2005**, 37, 425–455.
- (7) Yao, Z.; Bowick, M. J. Self-propulsion of droplets by spatially-varying surface topography. Soft Matter **2012**, 8, 1142–1145.
- (8) Li, H.; Yan, T.; Fichthorn, K. A.; Yu, S. Dynamic contact angles and mechanisms of motion of water droplets moving on nano-pillared superhydrophobic surfaces: A molecular dynamics simulation study. Langmuir **2018**, 34, 9917–9926.
- (9) Becton, M.; Wang, X. Controlling nanoflake motion using stiffness gradients on hexagonal boron nitride. RSC Adv. **2016**, 6, 51205–51210.
- (10) van den Heuvel, M. G. L.; Dekker, C. Motor proteins at work for nanotechnology. Science **2007**, 317, 333–336.
- (11) DuChes, B. J.; Doyle, A. D.; Dimitriadis, E. K.; Yamada, K. M. Durotaxis by human cancer cells. Biophys. J. **2019**, 116, 670–683.
- (12) Khang, G. Evolution of gradient concept for the application of regenerative medicine. Biosurface Biotribology **2015**, 1, 202–213.
- (13) Lo, C.-M.; Wang, H.-B.; Dembo, M.; Wang, Y.-L. Cell movement is guided by the rigidity of the substrate. Biophys. J. **2000**, 79, 144–152.

- (14) Pham, J. T.; Xue, L.; Del Campo, A.; Salierno, M. Guiding cell migration with microscale stiffness patterns and undulated surfaces. Acta Biomaterialia **2016**, 38, 106–115.
- (15) Lazopoulos, K. A.; Stamenović, D. Durotaxis as an elastic stability phenomenon. J. Biomech. **2008**, 41, 1289–1294.
- (16) Theodorakis, P. E.; Egorov, S. A.; Milchev, A. Stiffness-guided motion of a droplet on a solid substrate. J. Chem. Phys. **2017**, 146, 244705.
- (17) Chang, T.; Zhang, H.; Guo, Z.; Guo, X.; Gao, H. Nanoscale directional motion towards regions of stiffness. Phys. Rev. Lett. **2015**, 114, 015504.
- (18) Becton, M.; Wang, X. Thermal gradients on graphene to drive nanoflake motion. J. Chem. Theory Comput. **2014**, 10, 722–730.
- (19) Barnard, A. S. Nanoscale locomotion without fuel. Nature **2015**, 519, 37–38.
- (20) Palaia, I.; Paraschiv, A.; Debets, V. E.; Storm, C.; Šarić, A. Durotaxis of Passive Nanoparticles on Elastic Membranes. ACS Nano **2021**, 15, 15794–15802.
- (21) Tamim, S. I.; Bostwick, J. B. Model of spontaneous droplet transport on a soft viscoelastic substrate with nonuniform thickness. Phys. Rev. E **2021**, 104, 034611.
- (22) Bardall, A.; Chen, S.-Y.; Daniels, K. E.; Shearer, M. Gradient-induced droplet motion over soft solids. IMA J. Appl. Math **2020**, 85, 495–512.
- (23) Kajouri, R.; Theodorakis, P. E.; Deuar, P.; Bennacer, R.; Židek, J.; Egorov, S. A.; Milchev, A. Unidirectional Droplet Propulsion onto Gradient Brushes without External Energy Supply. Langmuir **2023**, 39, 2818–2828.
- (24) Style, R. W.; Che, Y.; Park, S. J.; Weon, B. M.; Je, J. H.; Hyland, C.; German, G. K.; Power, M. P.; Wilen, L. A.; Wettlaufer, J. S.; Dufresne, E. R. Patterning droplets with durotaxis. Proc. Natl. Acad. Sci. U.S.A. **2013**, 110, 12541–12544.

- (25) Theodorakis, P. E.; Egorov, S. A.; Milchev, A. Rugotaxis: Droplet motion without external energy supply. EPL **2002**, 137, 43002.
- (26) Hiltl, S.; Böker, A. Wetting Phenomena on (Gradient) Wrinkle Substrates. Langmuir **2016**, 32, 8882–8888.
- (27) Sadhu, R. K.; Luciano, M.; Xi, W.; Martinez-Torres, C.; Schröder, M.; Blum, C.; Tarantola, M.; Penič, S.; Iglič, A.; Beta, C.; Steinbock, O.; Bodenschatz, E.; Ladoux, B.; Gabriele, S.; Gov, N. S. A minimal physical model for curvotaxis driven by curved protein complexes at the cell's leading edge. bioRxiv **2023**, doi: 10.1101/2023.04.19.537490.
- (28) Feng, S.; Delannoy, J.; Malod, A.; Zheng, H.; Quéré, D.; Wang, Z. Tip-induced flipping of droplets on Janus pillars: From local reconfiguration to global transport. Sci. Adv. **2020**, 6, eabb5440.
- (29) Feng, S.; Zhu, P.; Zheng, H.; Zhan, H.; Chen, C.; Li, J.; Wang, L.; Yao, X.; Liu, Y.; Wang, Z. Three dimensional capillary ratchet-induced liquid directional steering. Science **2021**, 373, 1344–1348.
- (30) Theodorakis, P. E.; Amirfazli, A.; Hu, B.; Che, Z. Droplet Control Based on Pinning and Substrate Wettability. Langmuir **2021**, 37, 4248–4255.
- (31) Pismen, L. M.; Thiele, U. Asymptotic theory for a moving droplet driven by a wettability gradient. Phys. Fluids **2006**, 18, 042104.
- (32) Wu, H.; Zhu, K.; Cao, B.; Zhang, Z.; Wu, B.; Liang, L.; Chai, G.; Liu, A. Smart design of wettability-patterned gradients on substrate-independent coated surfaces to control unidirectional spreading of droplets. Soft Matter **2017**, 13, 2995–3002.
- (33) Sun, L.; Jing, D. Directional self-motion of nanodroplets driven by controlled surface wetting gradients. Phys. Fluids **2023**, 35, 052009.

- (34) Sun, Q.; Wang, D.; Li, Y.; Zhang, J.; Ye, S.; Cui, J.; Chen, L.; Wang, Z.; Butt, H. J.; Vollmer, D.; Deng, X. Surface charge printing for programmed droplet transport. Nat. Mater. **2019**, 18, 936–941.
- (35) Jin, Y.; Xu, W.; Zhang, H.; Li, R.; Sun, J.; Yang, S.; Liu, M.; Mao, H.; Wang, Z. Electrostatic tweezer for droplet manipulation. Proc. Natl. Acad. Sci. U.S.A. **2022**, 119, e2105459119.
- (36) Xu, W.; Jin, Y.; Li, W.; Song, Y.; Gao, S.; Zhang, B.; Wang, L.; Cui, M.; Yan, X.; Wang, Z. Triboelectric wetting for continuous droplet transport. Sci. Adv. **2022**, 8, eade2085.
- (37) Jin, Y.; Liu, X.; Xu, W.; Sun, P.; Huang, S.; Yang, S.; Yang, X.; Wang, Q.; Lam, R. H. W.; Li, R.; Wang, Z. Charge-Powered Electrotaxis for Versatile Droplet Manipulation. ACS Nano **0**, 0, null.
- (38) Zhang, K.; Li, J.; Fang, W.; Lin, C.; Zhao, J.; Li, Z.; Liu, Y.; Chen, S.; Lv, C.; Feng, X.-Q. An energy-conservative many-body dissipative particle dynamics model for thermocapillary drop motion. Phys. Fluids **2022**, 34, 052011.
- (39) Dundas, D.; McEniry, E. J.; Todorov, T. N. Current-driven atomic waterwheels. Nat. Nanotechnol. **2009**, 4, 99–102.
- (40) Regan, B. C.; Aloni, S.; Ritchie, R. O.; Dahmen, U.; Zettl, A. Carbon nanotubes as nanoscale mass conveyors. Nature **2004**, 428, 924.
- (41) Zhao, J.; Huang, J.-Q.; Wei, F.; Zhu, J. Mass transportation mechanism in electrically biased carbon nanotubes. Nano Lett. **2010**, 10, 4309–4315.
- (42) Kudernac, T.; Ruangsupapichat, N.; Parschau, M.; Maciá, B.; Katsonis, N.; Harutyunyan, S. R.; Ernst, K.-H.; Feringa, B. L. Electrically driven directional motion of a four-wheeled molecule on a metal surface. Nature **2011**, 479, 208–211.

- (43) ShklyaeV, O. E.; Mockensturm, E.; Crespi, V. H. Theory of carbomorph cycles. Phys. Rev. Lett. **2013**, 110, 156803.
- (44) Fennimore, A. M.; Yuzvinsky, T. D.; Han, W.-Q.; Fuhrer, M. S.; Cumings, J.; Zettl, A. Rotational actuators based on carbon nanotubes. Nature **2003**, 424, 408–410.
- (45) Bailey, S. W. D.; Amanatidis, I.; Lambert, C. J. Carbon nanotube electron windmills: A novel design for nanomotors. Phys. Rev. Lett. **2008**, 100, 256802.
- (46) Huang, Y.; Zhu, S.; Li, T. Directional transport of molecular mass on graphene by straining. Extreme Mech. Lett. **2014**, 1, 83–89.
- (47) Santos, F. D.; Ondarquist, T. Free-Running Droplets. Phys. Rev. Lett. **1995**, 75, 2972.
- (48) Lee, S. W.; Kwok, D. Y.; Laibinis, P. E. Chemical influences on adsorption-mediated self-propelled drop movement. Phys. Rev. E **2002**, 65, 9.
- (49) Daniel, S.; Chaudhury, M. K. Rectified motion of liquid drops on gradient surfaces induced by vibration. **2002**, 18, 3404–3407.
- (50) Brunet, P.; Eggers, J.; Deegan, R. D. Vibration-induced climbing of drops. Phys. Rev. Lett. **2007**, 99, 3–6.
- (51) Brunet, P.; Eggers, J.; Deegan, R. D. Motion of a drop driven by substrate vibrations. Eur. Phys. J.: Spec. Top. **2009**, 166, 11–14.
- (52) Kwon, O. K.; Kim, J. M.; Kim, H. W.; Kim, K. S.; Kang, J. W. A Study on Nanosensor Based on Graphene Nanoflake Transport on Graphene Nanoribbon Using Edge Vibration. J. Electr. Eng. Technol. **2023**, 18, 663–668.
- (53) Buguin, A.; Talini, L.; Silberzan, P. Ratchet-like topological structures for the control of microdrops. Appl. Phys. A: Mater. Sci. Process. **2002**, 75, 207–212.

- (54) Thiele, U.; John, K. Transport of free surface liquid films and drops by external ratchets and self-ratcheting mechanisms. Chem. Phys. **2010**, 375, 578–586.
- (55) Noblin, X.; Kofman, R.; Celestini, F. Ratchetlike motion of a shaken drop. Phys. Rev. Lett. **2009**, 102, 1–4.
- (56) Ni, E.; Song, L.; Li, Z.; Lu, G.; Jiang, Y.; Li, H. Unidirectional self-actuation transport of a liquid metal nanodroplet in a two-plate confinement microchannel. Nanoscale Adv. **2022**, 4, 2752–2761.
- (57) Barthlott, W.; Mail, M.; Neinhuis, C. Superhydrophobic hierarchically structured surfaces in biology: evolution, structural principles and biomimetic applications. Phil. Trans. R. Soc. A **2016**, 374, 2016019.
- (58) Badr, R. G. M.; Hauer, L.; Vollmer, D.; Schmid, F. Cloaking Transition of Droplets on Lubricated Brushes. J. Phys. Chem. B **2022**, 126, 7047–7058.
- (59) Button, B.; Cai, L.-H.; Ehre, C.; Kesimer, M.; Hill, D. B.; Sheehan, J. K.; Boucher, R. C.; Rubinstein, M. A Periciliary Brush Promotes the Lung Health by Separating the Mucus Layer from Airway Epithelia. Science **2012**, 337, 937–941.
- (60) Stukowski, A. Visualization and analysis of atomistic simulation data with OVITO—the Open Visualization Tool. Modelling Simul. Mater. Sci. Eng. **2010**, 18, 015012.
- (61) Kremer, K.; Grest, G. S. Dynamics of entangled linear polymer melts: A molecular-dynamics simulation. J. Chem. Phys. **1990**, 92, 5057.
- (62) Theodorakis, P. E.; Fytas, N. G. Microphase separation in linear multiblock copolymers under poor solvent conditions. Soft Matter **2011**, 7, 1038–1044.
- (63) Tretyakov, N.; Müller, M. Directed transport of polymer drops on vibrating superhydrophobic substrates: a molecular dynamics study. Soft matter **2014**, 10, 4373–86.

- (64) Everaers, R.; Karimi-Varzaneh, H. A.; Fleck, F.; Hojdis, N.; Svaneborg, C. Kremer–Grest Models for Commodity Polymer Melts: Linking Theory, Experiment, and Simulation at the Kuhn Scale. Macromolecules **2020**, 53, 1901–1916.
- (65) Rubinstein, M.; Colby, R. Polymer Physics; Oxford University Press, 2003; p 316.
- (66) Anderson, J. A.; Glaser, J.; Glotzer, S. C. HOOMD-blue: A Python package for high-performance molecular dynamics and hard particle Monte Carlo simulations. Computational Materials Science **2020**, 173, 109363.
- (67) Grest, G. S.; Murat, M. Structure of grafted polymeric brushes in solvents of varying quality: A molecular dynamics study. Macromolecules **1993**, 26, 3108–3117.
- (68) Murat, M.; Grest, G. S. Structure of a grafted polymer brush: a molecular dynamics simulation. Macromolecules **1991**, 24, 704–708.
- (69) Binder, K.; Milchev, A. Polymer brushes on flat and curved substrates: how computer simulations can help to test theories and to interpret experiments. J. Polym. Sci., Part B: Polym. Phys. **2012**, 50, 1515–1555.
- (70) Poma, A. B.; Guzman, H. V.; Li, M. S.; Theodorakis, P. E. Mechanical and thermodynamic properties of $\alpha\beta 42$, $\alpha\beta 40$, and α -synuclein fibrils: a coarse-grained method to complement experimental studies. Beilstein J. Nanotechnol. **2019**, 10, 500–513.

TOC Graphic

